JURNAL INFOTEL
VOL. 17, NO. 2, MAY 2025, PP. 418–439. DOI:10.20895/INFOTEL.V17I2.1218

RESEARCH ARTICLE

Performance Comparison of Three Modified Howland Current Source Circuits in Low-Cost Portable Bioimpedance Analyzer for Bio-Phantom Signal Acquisition

Eka Firmansyah[1] and Ridwan Wicaksono[2,*]

[1,2]Electrical and Information Engineering Departement, Faculty of Engineering, Universitas Gadjah Mada, Daerah Istimewa Yogyakarta 55281, Indonesia

*Corresponding email: ridwan.wicaksono@ugm.ac.id

Received: August 01, 2024; Revised: May 27, 2025; Accepted: May 27, 2025.

Abstract: Electrical impedance tomography (EIT), a method based on the bioimpedance analyzer (BIA) technique, supports recent advancements in gastric monitoring for telehealth applications. The challenge in providing a low-cost portable bioimpedance analyzer (p-BIA) is ensuring a stable current injection over diverse tissue conductivities within the abdominal cavity. The Howland current source (HCS), a current injector based on a commonly available operational amplifier (op-amp), has the potential to provide a solution. In this paper, three circuits based on HCS are investigated for application in p-BIA. Those are: a) triple amplifier Howland current source (TAHCS), b) mirrored Howland current source (MHCS), and c) composite mirrored Howland current source (CMHCS). Evaluation has been conducted based on the signal-to-noise ratio (SNR), the operating frequency range, and the output impedance's frequency response and stability. Due to its high SNR value (82.56 to 102.1 dB), broad operating frequency (500 Hz to 500 kHz), and consistent output impedance over the operating frequency (10 to 25 kΩ), CMHCS is a suitable option for realizing p-BIA in gastric monitoring-based EIT.

Keywords: composite mirrored Howland current source (CMHCS), electrical impedance tomography (EIT), Howland current source, mirrored Howland current source (MHCS), portable bioimpedance analyzer (p-BIA), triple amplifier Howland current source (TAHCS)

 ISSN: 2085-3688; e-ISSN: 2460-0997

1 Introduction

Recent advancements in telehealth gastric monitoring applications have increased attention to electrical impedance tomography (EIT), which is based on the bioimpedance analyzer (BIA), as a diagnosis method. The EIT presents a promising alternative for assessing the gastrointestinal (GI) tract due to its robustness against noise from cardiac electrical activity and its ability to provide rapid clinical evaluations compared to electrogastrogram (EGG) techniques [1]. Historically, EIT has been successfully applied in various biomedical applications. It has been used in breast cancer imaging [2] and lung monitoring [3]. However, gastric imaging faces additional difficulties due to the unclear conductivity distribution among abdominal organs, which is influenced by gastric volume and secretion responses, resulting in signal accuracy and image quality issues. It is stated in [4] that the electrical conductivity of nearby organs is quite similar, which results in a gastric conductivity distribution image generated by EIT buried in noise.

Several studies have investigated gastric motility using 2D/3D conductivity images obtained through transcutaneous electrical impedance measurements. It highlights the complexity of achieving high accuracy in low-cost portable bio-impedance analyzer (p-BIA) systems [5]. While it can not be categorized as a portable device, Yuan et al. [6] provided a theoretical framework for detecting fatty liver in human subjects using frequencies of 50-250 kHz and currents of 2-4 mA. This research portrays EIT devices as equipment that is not portable, consumes high electric power, and is expensive.

The main challenge in gastric EIT application is ensuring a stable current injection of the diverse tissue conductivities within the abdominal cavity. Therefore, several criteria must be considered when designing a current source for low-cost p-BIA. One key criterion in the current injection circuit topology is the output impedance. The current source circuit should be characterized with high output impedance to ensure accurate bioimpedance measurements [7, 8].

The current magnitude in the bioimpedance analyzer application should remain below the perception threshold of 1.0-1.2 mA, depending on the frequency as specified by IEC-60601 [9]. Enhanced Howland current source (EHCS) is a popular topology in this area. It offers a constant current for the generic current injection function and provides a solution for portable impedance analyzer systems that eliminates the need for complex circuitry. However, implementing EHCS with large load impedances is problematic due to current leakage issues. The output impedance should be in the order of megaohms to maintain constant current output independent of changes in load impedance [10]. As the current source must be capable of delivering a constant current across a wide range of load impedances to gastric organs, simplifying the modeling of the conversion formula from sensor voltage to varying impedance values, some alternative current source topologies need to be investigated. Another important criterion is adequate frequency range. For better tissue differentiation and more precise imaging, the electrical impedance properties of different tissues should be significantly distinct [11]. However, as stated in [4], the electrical conductivity of nearby gastric organs is quite similar, which hinders accurate EIT measurement. It has been found that frequencies around 100 kHz have the distinct advantage of minimizing artifacts caused by capacitive coupling between electrodes and the skin, resulting in cleaner and more reliable images [12], a finding also suggested in [11]. It is found that existing current source topologies, as stated in [8], frequently encounter performance issues at 100 kHz.

Researchers have evaluated voltage-controlled current sources (VCCS) as the current injector for portable bioimpedance studies. The topology has successfully enhanced the quality of gastric tumor imaging, promising safety, portability, and continuous monitoring [13]. However, the chosen topology achieved only 70 dB signal-to-noise ratio (SNR), whereas a minimum SNR of over 80 dB is recommended [14]. From this perspective, while providing an idea of how to achieve wideband and accurate current injection for bioimpedance measurement, the current injection method proposed by M. A. Kadir et al. [8] and [10] requires further investigation regarding the SNR quality. Most VCCS studies prioritize achieving high output impedance and stable constant current across various frequencies rather than ensuring a high SNR.

This paper aims to develop a current source for a low-power p-BIA system for gastric phantom data acquisition systems (DAS). Three modifications to the Howland current source (HCS) topology, enriching the approach of [10], are proposed. To achieve stable output impedance and high-range constant current, the evaluated Howland circuit topology is evaluated at frequencies between 1-100 kHz and load ranges of 1-25 kΩ, not only for their current injection stability but also their SNR quality. Finally, this study also employs an in vitro experiment using liver and stomach agar phantoms to compare the Euclidean distance of the portable BIA signal with that of a high-cost impedance analyzer.

2 Research Method

The research is conducted primarily in four linear steps, as depicted in Figure 1. Based on the requirements of p-BIA in gastro tomography, three research parameters are selected to indicate a suitable current injector topology: SNR, the operating frequency range, and the output impedance. Three current injection topologies based on the Howland circuit are chosen as current injector candidates: the Triple Amplifier Howland Current Source (TAHCS), the Mirrored Howland Current Source (MHCS), and the Composite Mirrored Howland Current Source (CMHCS). Those three topologies are created and tested one by one in the p-BIA test bed. The measurements are based on the three selected parameters. The measurement results are then compared.

2.1 Main Hardware System

A low-cost p-BIA designed for specific applications must strike a balance between performance and portability. For portable gastric monitoring, the system must handle alternative signal analysis approaches and effectively distinguish between organs, providing a constant current I_p to the load Z_{load}, operating within the gastric frequency range f, having high SNR, and maintaining high output impedance Z_o. VCCS circuit, such as the enhanced Howland current source (EHCS) in Figure 2, offers a constant current for a portable EIT system without a complex circuit [10].

Technically, the leakage current problem was solved by enlarging the feedback resistor (R_2, R_4) of Figure 2 to eliminate current flow from a feedback route to the load impedance Z_{load}. The Z_{load} is realized as an R-C model to represent gastric conductivity variations and the noise generated by peristalsis and acid secretion. These effects were modeled by adjusting the values of the resistive load and capacitive load.

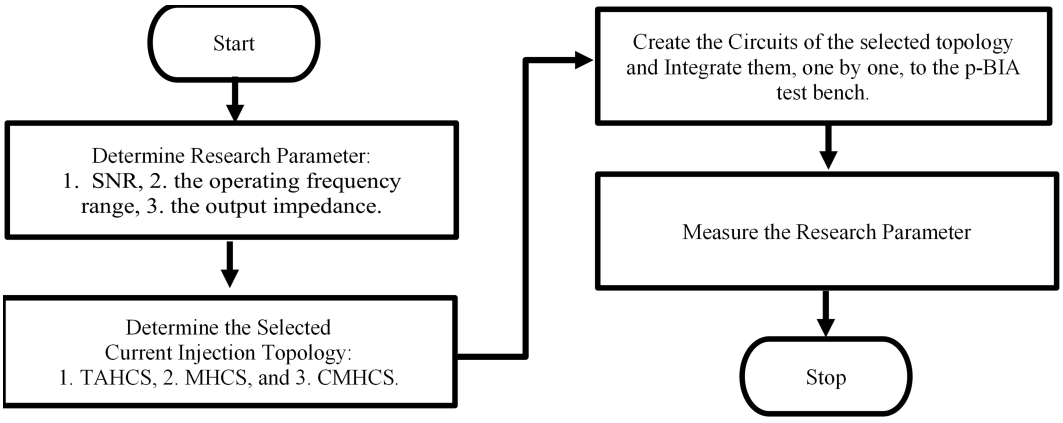

Figure 1: The research flowchart.

The current source in Figure 2 is part of a p-BIA for gastric monitoring, as illustrated in Figure 3. The device integrates a field-programmable gate array (FPGA) Xilinx Zynq 7010 SoC with a dual-core ARM-based microprocessor, in conjunction with the proposed modified current source, a second-order active filter, and a high-speed multiplexer. As a low-power portable device, the p-BIA is powered by a 3.7V 10,000 mAh lithium battery, which can be recharged via a standard micro-USB cable.

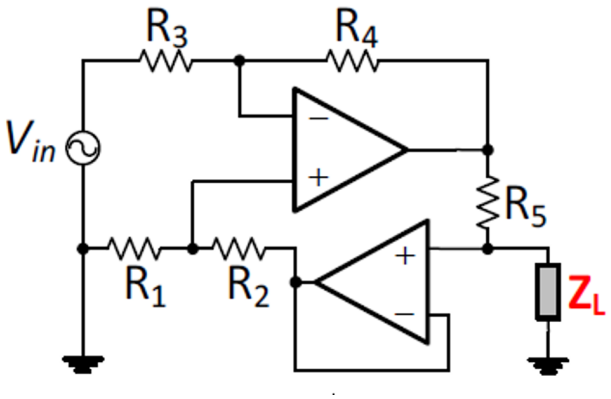

Figure 2: Enhanced Howland Current Source.

The p-BIA performs several critical functions: it generates a sinusoidal AC signal with a specific amplitude and frequency using a fast analog output. A low-pass filter first filters the signal and then converts it to a constant current signal via a VCCS. The signal is then directed to the abdominal area through a high-speed multiplexer and electrodes. The resulting signal from the interaction between the injected current and the bioimpedance is then acquired through a fast analog input. The DC offset in the acquired signal is removed using an active second-order high-pass filter (HPF). The analog output and input channels have 50 MHz analog bandwidth and a 125 MS/s sampler. Data are stored in

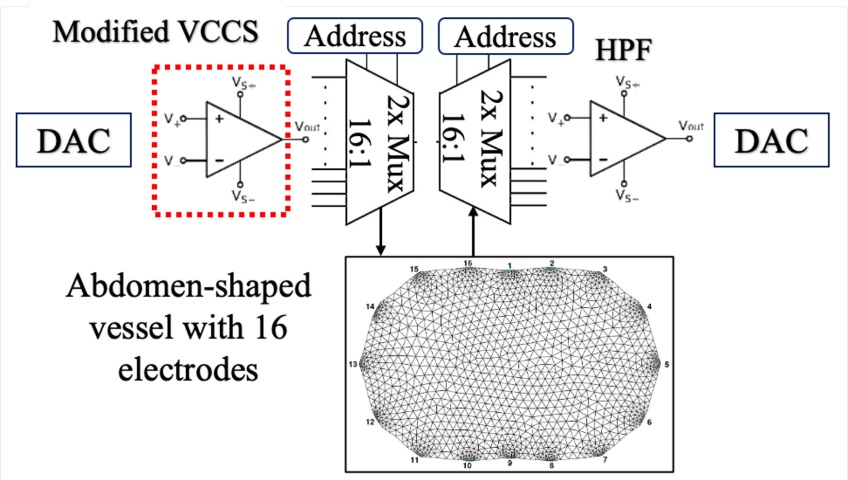

Figure 3: Portable bioimpedance analyzer (p-BIA).

16,384 16,384-sample signal buffer. A PC then processes these buffered signals through standard commands for programmable instrumentation (SCPI) via LAN or Wi-Fi. The gastric impedance influenced by its content varies in the minute order. Therefore, the measurement time should be on the order of seconds. Using SCPI, the proposed p-BIA acquires over 16 channels of electrodes in a few seconds and transmits data properly prepared for image reconstruction and analysis of the gastric boundary in phantom experiments.

2.2 Current Source Modification

The modified TAHCS topology is depicted in Figure 4. A TAHCS is based on triple operational amplifiers, which still exhibit low accuracy and repeatability for gastric impedance acquisition. TAHCS topology provides constant current and output impedance while the load impedance increases. The accuracy becomes unstable because the current output still flows back towards the positive terminal on the OPAMP. However, TAHCS serves as a basis for calculating a constant current source, as shown in Eq. (1).

$$i_{\text{out}} = \frac{1}{R_{2b}} \frac{R_4}{R_3} \left(\frac{R_{2a} + R_2 \frac{R_3}{R_4}}{R_{2a} + R_1} V_{in+} - V_{in-} \right) + \frac{R_4 R_1 - R_2 R_3}{R_3 R_{2b} (R_1 + R_{2a})} \tag{1}$$

Based on Kirchhoff's Current Law and assuming $V_{in-} = 0$, using the same value resistor on R_1, R_2, R_3, R_4, while $R_2 = R_{2a} + R_{2b}$ and the following relation $\frac{R_2}{R_1} = \frac{R_4}{R_3}$, Eq. (**??**) was simplified to Eq. (2).

$$i_{\text{outEHCS}} = \frac{R_4}{R_{2b} R_3} V_{\text{in}+} \tag{2}$$

The value of R_load affects the value of the output current of TAHCS. R_{2b} and R_load must be included as the total load injected by constant current. Suppose $R_{2b} = R_{\text{out}}$ is much smaller than $R_{2a} \approx R_2$ and $V_{\text{in}+}$ The output current was calculated by Eq. (3) has the same value as the input signal.

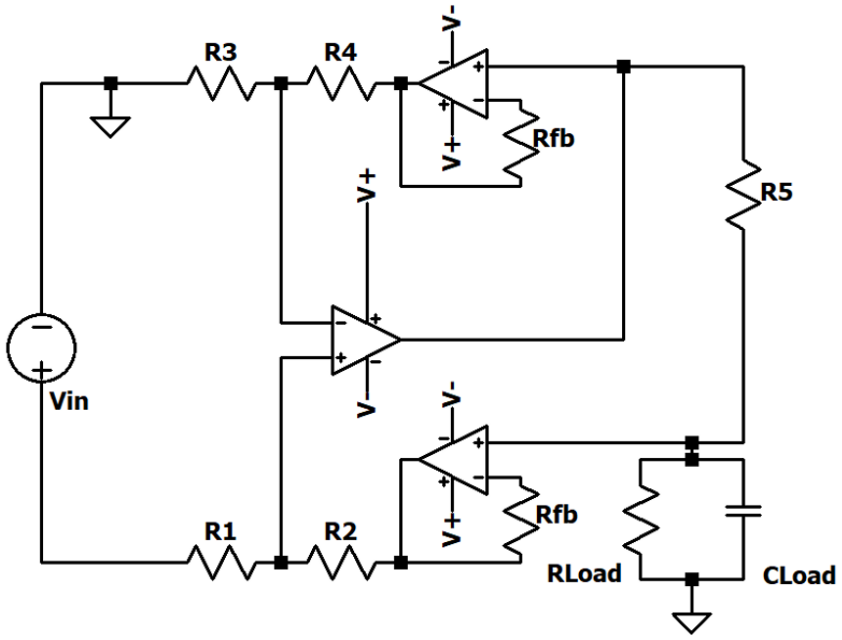

Figure 4: Triple amplifier Howland current source (TAHCS) topology modification.

$$i_{\text{out EHCS}} = \frac{R_4}{R_{\text{out}} R_3} V_{\text{in}} - i_{\text{drops}} \tag{3}$$

Higher load drives OPAMP to emanate an even greater voltage amplitude to perform constant current. However, the output voltage is limited by the maximum supply voltage ($V_{\max}$ OPAMP) of the OPAMP, which means that a constant current was achieved only over a specific load range. If $V_{\text{out}} < V_{\max}$ OPAMP then

$$i_{\text{outEHCS}} = \frac{V_{\text{out}}}{R_{\text{out}} + R_{\text{load}}} \tag{4}$$

If $V_{\text{out}} > V_{\max}$ OPAMP then

$$i_{\text{out EHCS}} = \frac{V_{\text{max OPAMP}}}{R_{\text{out}} + R_{\text{load}}} \tag{5}$$

The maximum load, driven by the constant current, depends on the maximum supply voltage. Otherwise, the current drops significantly. The maximum load supplied by the constant current was determined by combining Eq. (3) and Eq. (5),

$$R_{\text{loadEHCS}_{\max}} = \left(\frac{R_3 V_{\text{maxOPAMP}}}{R_4 V_{\text{in}}} - 1 \right) R_{\text{out}} \tag{6}$$

A large feedback resistor reduces the speed and precision of the circuit. Inserting a buffer into the feedback route with high-impedance input eliminates this backwardness.

The slew rate, bandwidth, settling time, and output noise density must be evaluated. However, the current range, the SNR, and the output impedance (Z_o) were not reported in detail. However, this circuit must be modified so that it can keep the peak current value (I_p) constant and precise at 1 mA.

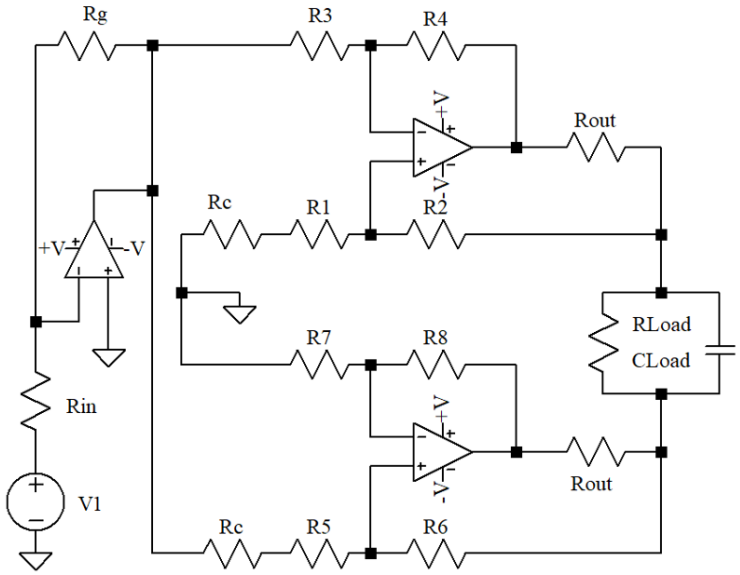

Figure 5: Mirrored Howland current source (MHCS) topology modification.

The MHCS topology is illustrated in Figure 5. This topology presents a technique for expanding the constant output current range by shifting the load's reference point (ground) to a mirrored topology. MHCS is composed of two opposite polarities, EHCS, connected in series. It generates an inverse voltage and symmetrical current concept on one side as a current injector and the other as a current suction. However, this circuit still presents some current imbalance problems due to the different input impedances on both sides. This difference in output current causes high values of the common mode voltage and reduces the output swing [15]. MHCS has equal output characteristics on both sides in the case $\frac{R_2}{R_{\text{out}}} = \frac{R_6}{R_{\text{out}}}$ where the ratio is equal. However, this technique generates an inconsistent current if resistor values 1-8 differ. In addition, using a resistor compensator of higher value $(R_c \geq R_{\text{out}})$ affects the smoothness of the current signal because resonance appears on each signal past the reference point $(0V)$. Suppose that resistor numbers 1-8 have the same value and the resistor compensator (R_c) is equal to 0, Eq. (7) shows the maximum load supplied $(R_{\text{loadMEHCS}_{\text{max}}})$ by the MHCS.

$$R_{\text{loadMEHCS}_{\text{max}}} = \left(\frac{R_3 V_{\text{maxOPAMP}}}{R_4 V_{\text{in}}} - 1\right) R_{\text{out}} + \left(\frac{R_7 V_{\text{maxOPAMP}}}{R_8 V_{\text{in}}} - 1\right) R_{\text{out}} \tag{7}$$

Figure 6 shows the CMHCS designed for p-BIA. Buffered feedback EHCS onto two opposite polarities connected serially on the forward and backward side against the load. The positive-negative voltage feedback of each side approaches the positive terminal of the buffer before connecting to the main OPAMP. The buffers block current feedback from the

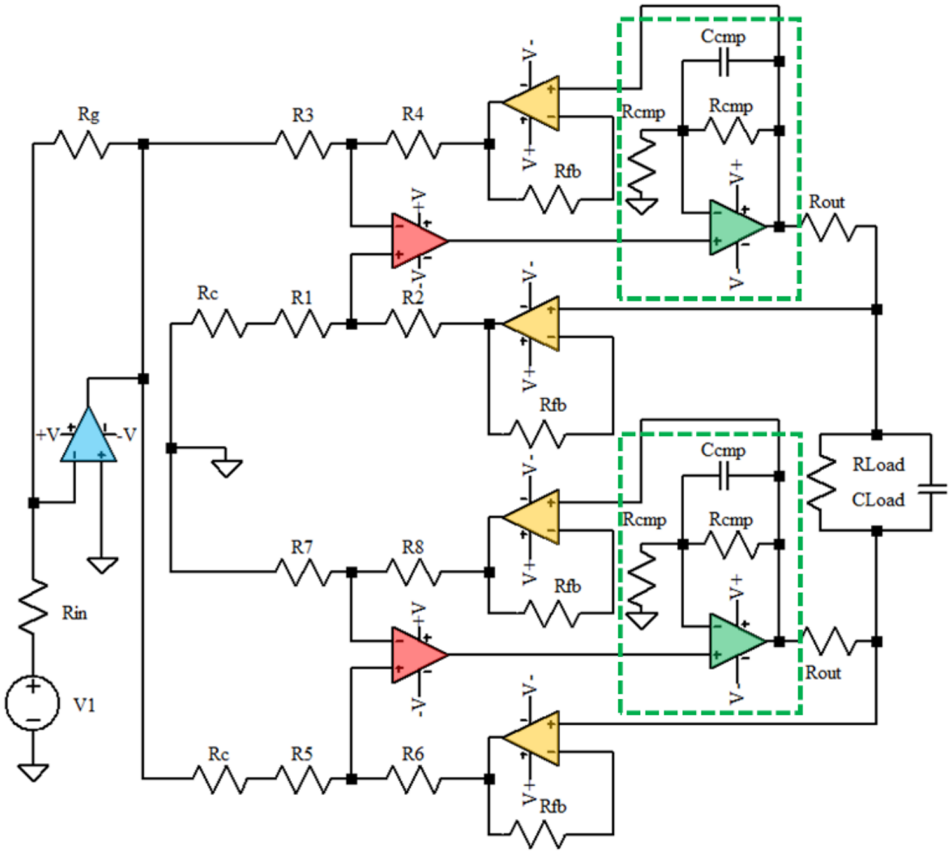

Figure 6: Composite Mirrored Howland Current Source (CMHCS) topology modification.

main OPAMP output, but still precisely supply the feedback voltage. The input impedance of the buffer is nearly infinite, and the output impedance is approximately a few ohms. The buffer output current replaces the primary OPAMP feedback current, which flows optimally and suppresses the current drop to the load. In addition, they help the main OPAMP to operate optimally and resolve impedance issues. The output impedance of the VCCS was calculated using the equation (8).

$$Z_o = \frac{V_{\text{load}_{\max}} - V_{\text{load}_{\min}}}{I_{\text{load}_{\max}} - I_{\text{load}_{\min}}} = \frac{V_{\text{load}_{\max}} - V_{\text{load}_{\min}}}{\frac{V_{\text{load}_{\min}}}{R_{\text{load}_{\min}}} - \frac{V_{\text{load}_{\max}}}{R_{\text{load}_{\max}}}} \tag{8}$$

In the basic concept of VCCS, an inverting op-amp also functions as a VCCS. Besides that, an additional inverting amplifier allows the user to calibrate the input gain ($G = -\frac{R_G}{R_{\text{in}}}$). Adding the buffer at the output and feedback lines represents a composite circuit. It trades speed for swing and reduces bias current output. The output signal from the Howland circuit drives the OPAPM composite and amplifies the output signal with unity gain. Finally, a parallel resistor (R_{load}) and capacitor (C_{load}) were used as load models (Z_{load}). The maximum supplied load ($Z_{\text{load}_{\max}}$) of the developed VCCS was determined by Eq. (9).

$$Z_{\text{load}_{\max}} = 2R_{\text{out}} \left(\frac{R_{\text{in}}}{R_G} \frac{V_{\text{maxOPAMP}}}{V_{\text{in}}} - 1 \right) \tag{9}$$

A dual low-power OPAMP called LT6275 provides ample slew rate and extensive output swing capability [9]. This chosen OPAMP provides excellent settling characteristics (40-185 ns) with a high slew rate (2200 $V/\mu s$), 110 dB of common-mode rejection ratio (CMRR), and a single-stage design. By using dual supply $15V$ on the mirrored side, the magnitude of the driving voltage of the OPAMP is initially limited to twice that of the supply voltage. It is highly possible to provide a wideband, large composite amplifier of the current source that performs stability with any resistive and capacitive load. The composite amplifier enables a giant output swing at high frequencies with relatively low power dissipation.

2.3 Signal Analyzer, Multiplexer, and Analog Filter

Several conventional scanning methods exist to generate signals in the tomography system, including adjacent, opposite, cross, adaptive, and quasi-adjacent [16, 17]. The quasi-adjacent method was selected because it performs Real (Z) two times higher, Imaginer (Z) ten times higher, and has a broader sensitivity map area, which successfully eliminates negative resistance at higher frequencies and provides a constant spatial image. The 4-point probes method has been employed as an EIT measurement technique, utilizing separate pairs of current-injecting and voltage-sensing electrodes to achieve more accurate measurements.

To acquire the measurement signal, a fast 14-bit signal analyzer, the LTC2145, was implemented. It is possible to obtain 16k samples with this IC. This IC facilitates higher resolution and reconfigures by changing the decimation value. The decimation value defines the number of sampling rates that benefit from reducing buffer length and measurement time, as shown in Table 1.

The multiplexer (MUX) circuit configuration was arranged following this scanning method. Due to the switching speed limitation and the size of a conventional relay, the proposed MUX circuit reduces the connection from the current injector and measurement

Table 1: Sampling rate configuration of LTC2145

DECIMATION	**SAMPLING RATE** [S/S]	**BUFFER** [S]
1	125M	131.072u
8	15.6M	1.049m
64	1.9M	8.389m
1024	122.0k	134.218m
8192	15.2k	1.074
65536	7.6k	8.59

probe to 16 channels of electrodes. Moreover, the 74HC4067, a conventional MUX used in the EIT system [27] with a 5V operation voltage and a transition time of 400nS–1000nS, performs poorly because it operates on a single supply voltage. The conventional MUX causes the signal in the negative region to be cut off and not gain in full. Based on the 16-channel MUX comparison, the ADG1406, which has a $15V$ operation voltage and a 160 nS to 260 nS transition time, is selected to deliver a faster acquisition time in an environment temperature of 25 C. The proposed MUX operates in dual supply, allowing signals in the negative region to be collected without interruption. ADG1406 has a low leakage current, ranging from 0.01nA to 0.5nA. Compared to the common 74HC4067, the ADG1406 has greater voltage compliance, faster transition times, and lower current leakage.

The measurement signals from this method are filtered with a high-pass filter (HPF). Then, the OPAMP amplifies the difference between 2 voltages, making this operational amplifier circuit a signal subtractor. Measurement of biological impedance yields an output AC signal response when an AC signal is applied as input. The output signal is accompanied by a DC offset, which makes the signal prone to error when measured directly by the ADC device. A signal processing needs to be done to eliminate the occurring DC offset. The amount of DC offset depends on the conductivity value of the object being measured. DC offset noise occurs at the DC frequency, ideally 0 Hz, resulting in a floating signal with a reference value that is not equal to 0. Because these measurements are focused on a specific frequency range, a signal filter must be applied to eliminate interference at low frequencies while filtering white noise at high frequencies.

A combination of an active low-pass and high-pass filter is applied to this work. The active filter was chosen because the passive filter is insufficient to filter out noise in low-conductivity objects. Additionally, the active filter utilizes an opamp to stabilize the current and amplify the signal. Because the frequency range of the human body is between 5 kHz and 15 kHz, the Sallen-Key Filter topology effectively overcomes the DC offset and noise in the output signal. After passing the cutoff frequency limit, the composite mirrored Howland current source (CMHCS) topology cuts the signals into the unwanted frequency range. Adjusting the resistor and capacitor values according to the HPF cut-off frequency equation determined the cut-off frequency. The HPF gain was calculated based on Eq. (10) below to determine the amplification of the filtered signal.

$$f_{c_{\mathrm{HPF}}} = \frac{1}{2\pi\sqrt{R_1 R_2 C_1 C_2}}; G_{\mathrm{HPF}} = \frac{R_3 + R_4}{R_3} \tag{10}$$

2.4 Phantom Model

Table 2 provides detailed information on the conductivity values of various abdominal tissues, which are essential to create a realistic abdomen phantom for the evaluation of the EIT. The conductivity values are measured in S/m (Siemens per meter) and represent the electrical properties of each tissue type. Using these conductivity values, researchers adjust the composition of the phantom materials to match the electrical properties of the actual tissues closely. For example, a mixture with a higher concentration of saline mimics muscle tissue, while a mixture with a lower concentration represents fat tissue. This approach ensures that the phantom provides a realistic model for testing and calibrating EIT systems.

The experimental agar phantom and human body measurements have been reported to provide both a theoretical and a conditional framework. Creating a gastric phantom for Electrical Impedance Tomography (EIT) evaluation involves designing a model that accurately replicates the anatomical shape and electrical properties of the human stomach. This process begins with the selection of materials such as agar, saline, and conductive gels, chosen for their ability to mimic the conductivity of gastric tissues. A mold, typically produced using 3D printing technology based on anatomical data, is used to shape the phantom. An agar-saline mixture is prepared with the required conductivity, poured into the mold, and allowed to solidify as shown in Table 3. Electrodes are embedded within the mold before the gel sets, replicating the placement of electrodes in an actual EIT setup.

To simulate gastric conditions such as peristalsis and acid secretion, regions with varying conductivities are created within the phantom by adjusting saline concentrations or embedding fluid-filled bladders. Once the phantom has solidified, its electrical properties are measured and adjusted as necessary to match those of human gastric tissues. The final step involves validating the phantom by connecting it to the EIT system and conducting tests to ensure accuracy and reliability.

Table 2: Abdomen tissues conductivity

NO	TISSUE NAME	CONDUCTIVITY [σ]
1	Skin Wet	0.001
2	Fat	0.0234
3	Spinal Cord	0.0321
4	Liver	0.0455
5	Spleen	0.1071
6	Cartilage	0.1753
7	Muscle	0.3343
8	Gastric	0.5273
9	Gallbladder	0.9001

2.5 Evaluation Method

To evaluate the output impedance (Z_o) performance, three different load resistors were examined. The two different load voltages were measured, corresponding to the nonload conditions V_{open} and the loaded conditions V_{load}. Then, the initial impedance Z_{o} was calculated according to Eq. (11).

Table 3: Phantom's electrical properties

No	Phantom	Material	Conductivity [S/M]	Boundary Area [MM^2]
1	Liver	Agar	0.148	6305
2	Low gastric content	Agar	0.254	2448
3	High gastric content	Agar	2.15	2448
4	Gastric Boundary Tissue	Agar	0.254	2205
5	Spinal cord	Acrylic	≈ 0	20
6	Human Normal Liquid	Saline Water	1.724	38692

$$Z_o = R_{\text{load}} \left(\frac{V_{\text{open}}}{V_{\text{load}}} - 1 \right) \tag{11}$$

SNR measurement is the standard for quantifying the performance of measurement devices. SNR is considered relevant for measuring human organs and has a minimum value of 80 dB. All four VCCS modifications have met these criteria. The signal-to-noise ratio is defined as the ratio of the power spectral density (PSD) of a signal (meaningful information) to the power of the background noise (white noise). The final SNR is calculated by Eq. (12), based on the mean of the peak-to-peak amplitude of the whole up-state FFT signal $P2P_{\text{up}}$, and the SD mean of the entire down-state FFT signal STD_{down}.

$$SNR = P_{\text{signal[dBm]}} - P_{\text{noise[dBm]}} \tag{12}$$

Data analysis compares 1) output impedance stability, 2) constant current performance, and 3) signal-to-noise ratio obtained from the p-BIA and the high-cost impedance analyzer. Moreover, the similarity of the two signals is evaluated by measuring the Euclidean distance value. The smaller the value of the Euclidean distance, the more similar it is to the reference signal. Euclidean distance is used to analyze the signal similarity and identify the best modification among the three proposed topologies. The analysis aims to validate the performance of the p-BIA against the high-cost analyzer, providing insights into impedance variations under different mimic gastric conditions and identifying potential areas for improvement in the p-BIA device for clinical applications.

3 Experiments

3.1 Experimental Setup

Three modifications of the current source topology were evaluated by examining their ability to provide a constant current to a load consisting of a pure resistor. The current used to measure gastric content is 1 mA. This current was agreed to be the optimal current that did not violate the IEC regulations. Furthermore, if the current injection is too small, the measured response signal is also too small, affecting the accuracy of the ADC reading. Pure resistors with a value of 100-100k are sufficient to represent impedance in the cross-section of the abdominal area, so that the resistor's range is used to validate the ability of the VCCS. Figure 7 shows the experimental setup of a high-cost impedance analyzer

used in in-vitro experiments. In vitro experiments with gastric phantoms are designed to simulate and study the physiological and electrical properties of the human stomach in a controlled laboratory environment. A gastric phantom typically mimics the anatomical and functional characteristics of the stomach, allowing researchers to conduct experiments without involving human or animal subjects.

Figure 8 shows the gastric phantom evaluation based on p-BIA. Both the proposed p-BIA and the high-cost impedance analyzers operate on 16 electrode channels and measure the cross-sectional gastric area by implementing the 4-point probe method. This method produces 208 measurements per frame according to the independent measurement, the total number of measurements, and the total number of channels. A quasi-adjacent switching method consecutively injected all electrodes with a constant current of 1 mA. Data collection from 16 electrode settings for gastric emptying measurement differs from conventional data collection. Four electrodes located in the epigastric region are used to collect data on changes in conductivity in the stomach. The impedance data from each electrode were replaced with the average data yield of each electrode at each measurement.

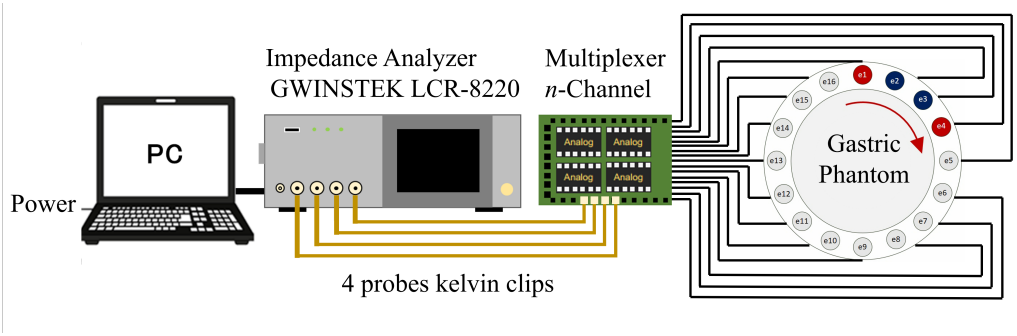

Figure 7: Experimental setup of high-cost impedance analyzer in in-vitro experiments.

Three phantom measurements have been confirmed using an impedance analyzer (IA) IM3570 and p-BIA. IM3570 represents a single, non-wearable, high-power device that consumes a 150 VA power supply. The proposed device represents a low-power wearable device (148 mm $\times$ 80 mm $\times$ 55 mm) that consumes an 8.15 VA power supply. A normal human liquid fills the vessel as background (1.724 S/m). In case 1, a liver phantom was placed in the vessel. In case 2, a high-conductivity (2.15 S/m) gastric content phantom was put into the vessel. In case 3, several phantoms were placed in the vessel: liver, gastric boundary tissue, low-conductivity gastric content (0.254 S/m), and acrylic (representing the spinal cord). The electrode boundary arrangement is distributed clockwise to form an EIT image that approaches the CT scan image regarding the 2D cross-sectional image of the abdominal organ.

3.2 Phantom Fabrication

Figure 9 shows the phantom fabrication process. The process of preparing a gastric phantom for in vitro experiments involves several steps. The procedure begins with constructing the phantom from conductive materials that mimic the electrical properties of stomach tissue. First, NaCl and agarose are weighed and mixed with distilled water. The mixture is

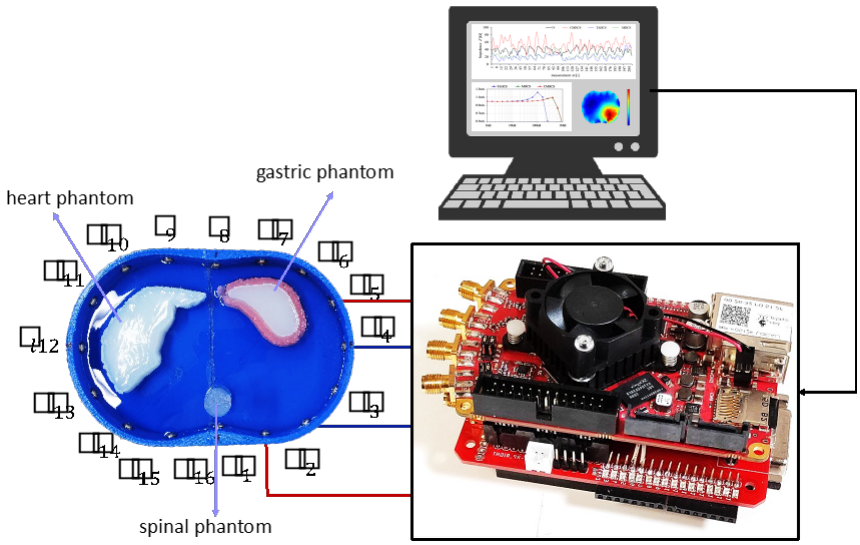

Figure 8: Gastric phantom evaluation by p-BIA.

then heated until it reaches a boil. Once boiling, the mixture is poured into an organ mold and stored in the refrigerator until it hardens. After hardening, the agarose, which simulates organ tissue, is placed into a phantom chamber. Finally, a NaCl solution, representing the conductivity of fat, is poured into the chamber. P-BIA evaluated the prepared phantom signal in a controlled laboratory environment to determine the electrical properties of the gastric.

In the in-vitro experiment using a gastric phantom, electrodes are embedded within the phantom, and it is connected to both a portable Bioelectrical Impedance Analysis (p-BIA) device and a high-cost impedance analyzer. The phantom is kept at a constant temperature to simulate body conditions. The experiment involves calibrating both impedance analyzers and a series of impedance measurements at various frequencies and locations on the phantom. Different gastric conditions, such as fasting and postprandial states, are simulated by adjusting the conductivity of the phantom material.

4 Results

4.1 Output Impedance Stability

Figure 10 shows the output impedance stability of (a) TAHCS, (b) MHCS, and (c) CMHCS. The provided graphs illustrate the impedance characteristics of three different high-capacitance supercapacitors when subjected to various load samples Zs at different frequencies ranging from 100 Hz to 1 MHz. Each graph depicts the impedance response for load resistances of 1 kΩ, 5 kΩ, 10 kΩ, and 25 kΩ, which are represented by the cyan, red, blue, and green curves, respectively. The output impedance of TAHCS, as shown in Figure 10 (a), decreases significantly as the frequency increases from 100 Hz to 1 MHz. It

Figure 9: Phantom fabrication process.

produces an output impedance of 7.7 MΩ at 100 Hz and drops sharply as the frequency increases when connected to a 1 kΩ load. A more gradual decrease in the output impedance is produced when the circuit is loaded with 5 kΩ, 10 kΩ, and 25 kΩ loads. It indicates that the TAHCS has a higher initial impedance and frequency-dependent response. At higher frequencies, the impedance values of all load samples converge, suggesting a similar performance across different loads.

The output impedance of MHCS, as shown in Figure 10 (b), follows a similar trend to TAHCS, but with slightly lower initial impedance values. It produces 7 MΩ output impedance at 100 Hz and decreases as the frequency increases when connected to 1 kΩ load. A more consistent decline in output impedance occurs when the circuit is loaded with the 5 kΩ, 10 kΩ, and 25 kΩ loads. The output impedances converge at higher frequencies, indicating the MHCS's capability to stabilize impedance across varying loads at elevated frequencies. The output impedance of CMHCS, as shown in Figure 10 (c), exhibits a distinct impedance profile. Its initial value is only 4.4 MΩ at 100 Hz when loaded with a 1 kΩ load, which is the lowest compared to TAHCS and MHCS. The impedance then decreases steadily across the frequency range—the trend is consistent with the 5 kΩ, 10 kΩ, and 25 kΩ loads. The impedance consistency across the frequency spectrum highlights its potential stability and reliability under different loading conditions.

4.2 Constant current performance

Figure 11 (a) shows the constant current performance of the proposed current source topologies. The provided graphs compare the performance of TAHCS, MHCS, and CMHCS in terms of constant current range. The figure shows the constant current range

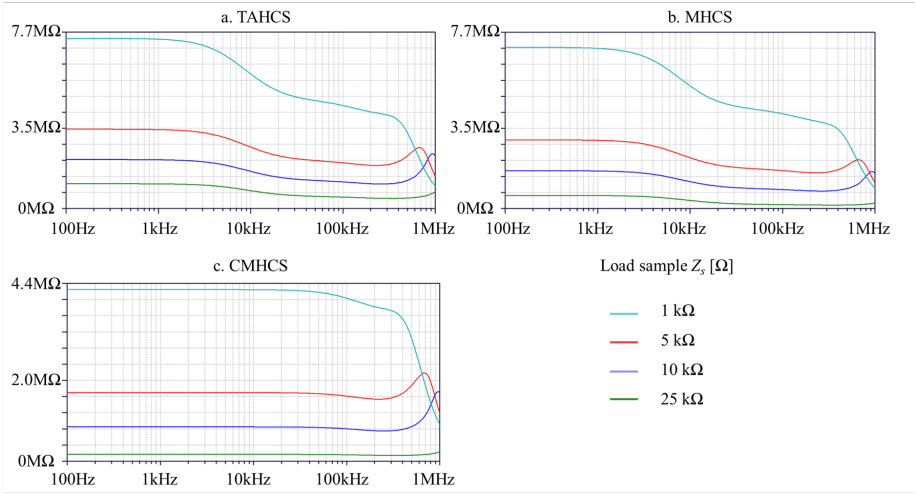

Figure 10: shows the output impedance stability of (a) TAHCS, (b) MHCS, (c) and CMHCS.

as a function of load impedance (Z). TAHCS displays a sharp increase in current as the load increases, peaking around 100 k before dropping dramatically near 1 MΩ. In contrast, MHCS and CMHCS maintain a more stable current range. However, CMHCS increases slightly but then stabilizes, which indicates better stability across varying load conditions.

4.3 Signal-to-Noise-Ratio Performance (SNR)

Figure 11 (b) pictures the SNR performance of the proposed current source topology as a function of conductivity [S/m]. TAHCS consistently exhibits the lowest SNR values across the conductivity range, maintaining a level around 70-80 dB, indicating poorer noise performance. MHCS and CMHCS show higher and relatively similar SNR values, starting around 110 dB and gradually decreasing to about 90 dB as conductivity increases. MHCS and CMHCS offer better noise performance and are more effective in maintaining a high SNR across different conductivity levels, making them more suitable for applications requiring high signal integrity. CMHCS has an SNR performance of 87.94 - 102.10 dB on a conductivity range of 0.1 - 10.0 S/m, with an average SNR of 95.69 dB. The CMHCS indicates the best modification for measuring the gastric emptying process.

5 Discussion

5.1 Static Bio-Phantom Signal Similarity

A comparison of bio-phantom signal acquisition over different current source topologies is illustrated in Figure 12. An IM3570 impedance analyzer (IA) serves as the reference for signal acquisition. The figure provides impedance Z measurements over 208 samples for four different signals: IA (black solid line), CMHCS (red dashed line), TAHCS (blue dashed

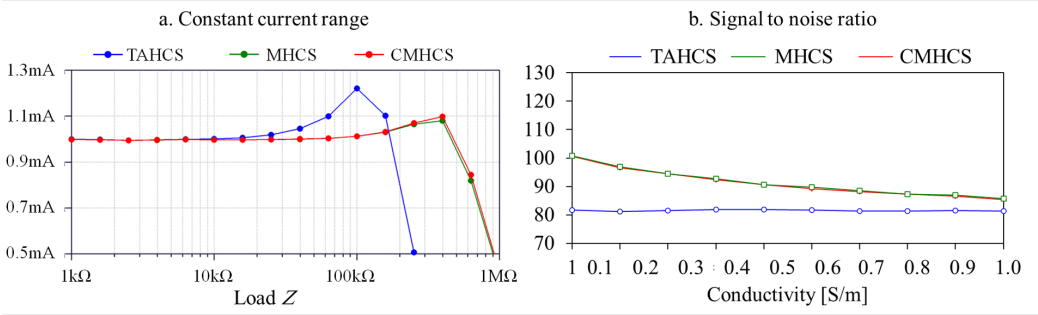

Figure 11: (a) Constant current and (b) SNR performance between of TAHCS- MHCS-CHMCS.

line), and MHCS (green dashed line). The impedance values shown (between 0 and 100Ω) figure out each topology's performance relative to the reference IA signal.

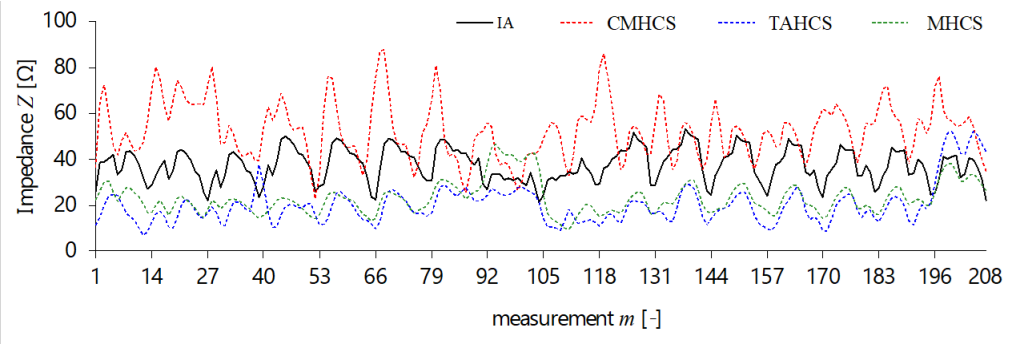

Figure 12: Comparison of gastric myoelectric signal with different current source development.

The CMHCS (red dashed line) exhibits higher impedance values with noticeable fluctuations throughout the measurement range. Despite these fluctuations, the correlation coefficient indicates that the pattern closely follows the IA. The peaks and troughs in the CMHCS signal are more pronounced, suggesting a higher sensitivity to measurement conditions or potential instability changes. The TAHCS (blue dashed line) shows lower impedance values than CMHCS and follows a more stable pattern with less pronounced peaks and troughs. TAHCS offers a more consistent impedance performance, closely matching the behavior of the IA signal, as confirmed by the perfect correlation coefficient. The MHCS (green dashed line) also demonstrates stability, with its impedance values closely aligning with the IA signal, especially in the mid-range of the measurements. The nearly perfect correlation coefficient confirms the strong alignment between the MHCS signal and the IA reference, indicating reliable and consistent performance under similar conditions.

Euclidean distances of the three proposed topologies compared to the IA signal are shown in Figure 13. The depicted parameter shows the overall difference between the

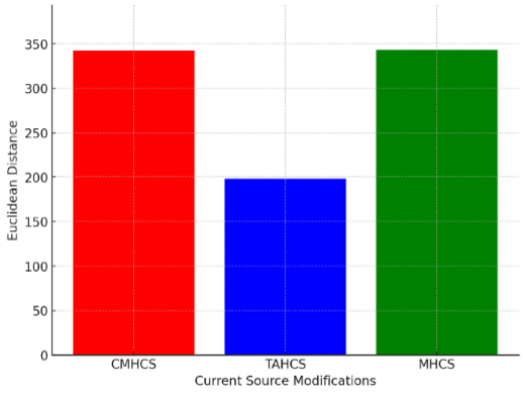

Figure 13: Euclidean distance of modified current source based on phantom signal.

impedance values of the IA compared to CMHCS, TAHCS, and MHCS across the measurements. The CMHCS has an Euclidean distance of approximately 344.75, which indicates moderate deviation from the IA reference signal. Although CMHCS produces a relatively consistent pattern, it does not align closely with the IA. TAHCS performs better as indicated by the smallest Euclidean distance of approximately 204.33. It makes the impedance behavior of TAHCS most similar to that of IA. The MHCS (green bar) has the greatest Euclidean distance of approximately 373.36. This distance makes MHCS the least accurate in replicating the IA. While TAHCS produces the smallest Euclidean distance to the IA, it is essential to consider other performance metrics and application-specific requirements when choosing the best current source modification for a particular use case.

Figure 14 shows the mean and standard deviation of impedance for the proposed current source topologies. The graph illustrates the mean and standard deviation of impedance compared to the IA signal. The mean impedance of the IA signal is around 30Ω, serving as the reference point. The mean impedance for CMHCS is approximately 60Ω, indicating it generally operates at higher impedance levels than the IA signal. TAHCS shows a mean impedance close to the IA signal, around 40Ω, suggesting a closer alignment with the reference. MHCS has a mean impedance of about 20Ω, indicating it operates at lower impedance levels than the IA signal.

The small standard deviation value suggests consistent performance with minimal variation around the mean. CMHCS exhibits a higher standard deviation, indicating more significant variability in impedance. CMHCS is more sensitive to load changes, which may benefit applications requiring dynamic response but could result in less stability. The standard deviation for TAHCS is moderate, indicating a balance between stability and adaptability. Its consistency makes it suitable for applications requiring stable performance. MHCS has the smallest standard deviation, indicating the most stable and consistent impedance. This stability makes it suitable for applications requiring minimal load variation.

The high mean impedance and significant standard deviation highlight the topology's responsiveness to load variations. It could be advantageous for applications requiring high sensitivity and dynamic range, but may be less ideal for scenarios that require consistent impedance. With a mean impedance close to IA and a moderate standard deviation,

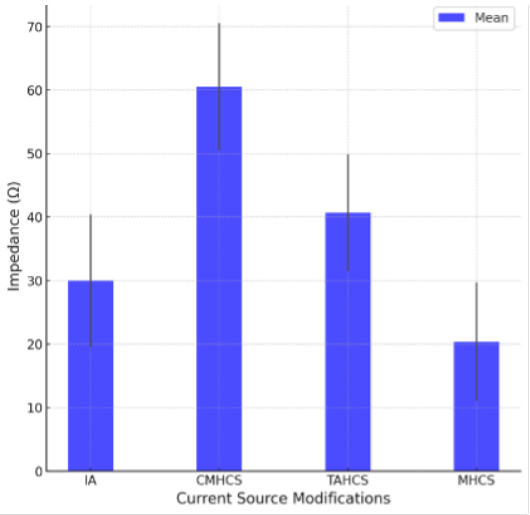

Figure 14: Mean and standard deviation of impedance for different current source modification.

TAHCS offers a good balance, making it suitable for various applications. It combines stability with enough adaptability to handle varying loads effectively. The lower mean impedance and the smallest standard deviation emphasize its stability. MHCS is ideal for applications requiring consistent, low-impedance performance with minimal variability.

CMHCS exhibits high responsiveness and variability, making it suitable for applications that require dynamic impedance adjustments, but less ideal for those that need consistent performance. TAHCS offers a balanced performance with moderate stability and adaptability, making it suitable for a wide range of applications. MHCS offers the most stable and consistent performance with the lowest variability, making it ideal for applications that require minimal impedance fluctuations. This quantitative analysis, combined with the visual representation of the mean and standard deviation, provides a comprehensive understanding of the performance of CMHCS, TAHCS, and MHCS in terms of load impedance variation.

5.2 Implementation for Dynamic Gastric Impedance in the Human Body

Dynamic gastric impedance refers to the variability in electrical impedance measurements within the gastric system, influenced by physiological processes such as peristalsis, gastric emptying, and varying gastric content. The impedance signals reflect changes in the stomach's contents and wall movements, providing valuable insights into gastric motility and the rates of emptying. In studies with an empty gastric phantom, homogeneous impedance signals are consistently recorded over 50 measurements. These measurements exhibit a standard deviation of less than 0.1, indicating the high repeatability and stability of p-BIA (Phase-sensitive Bioelectrical Impedance Analysis) signal acquisition. Such stability is essential because an inconsistent current source with conductivity below 1 S/m is unsuitable

for gastric emptying monitoring systems. Repeatable and stable signal acquisition is critical for accurately tracking gastric processes and ensuring reliable data interpretation.

The performance of CMHCS, characterized by its high mean impedance and significant variability, makes it well-suited for applications involving dynamic impedance variation, such as monitoring gastric activity in the human body. The human gastric system experiences continuous and often rapid changes in impedance due to peristalsis, varying contents, and different physiological states. CMHCS's ability to respond swiftly to these changes, with its high sensitivity and adaptability, ensures that CMHCS accurately tracks and reflects real-time variations in gastric impedance. CMHCS's capability is crucial for precise monitoring and diagnostic applications where capturing transient events and rapid fluctuations in impedance is essential.

In contrast, TAHCS, with its moderate mean impedance and balanced performance, offers a more stable response with less fluctuation than CMHCS. While TAHCS still handles dynamic variations, its performance may not be as responsive as CMHCS in capturing rapid changes in gastric impedance. However, the stability and moderate adaptability of TAHCS make it suitable for applications where a balance between sensitivity and consistency is needed. For instance, in scenarios where moderate variations are expected and high stability is required, TAHCS provides a reliable solution. It still offers valuable insights into gastric activity but may not capture the full extent of rapid impedance changes as effectively as CMHCS.

MHCS, on the other hand, with its lower mean impedance and minimal variability, is the most stable and consistent among the three. While MHCS stability is beneficial for applications requiring constant and reliable measurements with minimal fluctuation, it may not be as effective in environments with significant dynamic variations, such as the human gastric system. MHCS's limited responsiveness to rapid impedance changes may result in missing transient events or providing less detailed monitoring of dynamic physiological processes. Therefore, MHCS may be less suitable for monitoring gastric impedance compared to CMHCS and TAHCS, as it prioritizes stability over adaptability to rapid changes.

6 Conclusion

Three current injection topologies, (a) triple amplifier Howland current source (TAHCS), b) mirrored Howland current source (MHCS), and c) composite mirrored Howland current source (CMHCS), have been evaluated to realize a low-cost portable bioimpedance analyzer (p-BIA) in telehealth gastric monitoring electrical impedance tomography (EIT) application. Stable current injection over diverse tissue conductivities within the abdominal cavity is the main challenge. A current injector with an over 80 dB SNR, a broad operating frequency range, and stable output impedance across frequencies is the key to alleviating the challenge. Measurement with an impedance analyzer (IA) as the reference and a gastric phantom model over three proposed current injector topologies created using the LT6275 opamp results in the conclusion that the CMHCS topology is a good option for realizing p-BIA in gastric monitoring-based EIT. The chosen topology is characterized by a high SNR value (82.56 to 102.1 dB), a broad operating frequency range (500 Hz to 500 kHz), and a consistent output impedance across the operating frequency (10 to 25 kΩ). The results will serve as the foundation for further development of the p-BIA for telehealth gastric monitoring applications.

Acknowledgments

The authors would like to thank the Electrical and Information Engineering Department at Universitas Gadjah Mada for providing the facilities to conduct this research. Also, thanks to Alfian Daffa Baihaqi, who provided illustration images in this manuscript.

References

[1] R. Wicaksono, P. N. Darma, A. Inoue, H. Tsuji, and M. Takei, "Wearable sectorial electrical impedance tomography and k-means clustering for measurement of gastric processes," *Measurement Science and Technology*, vol. 33, p. 094002, Sept. 2022.

[2] J. Hu and M. Soleimani, "Combining multiple boundary shapes in deformable eit a potential use in breast imaging," *IEEE Sensors Letters*, vol. 4, pp. 1–4, Apr. 2020.

[3] D. Maciejewski, Z. Putowski, M. Czok, and J. Krzych, "Electrical impedance tomography as a tool for monitoring mechanical ventilation. an introduction to the technique," *Advances in Medical Sciences*, vol. 66, pp. 388–395, Sept. 2021.

[4] K. Sakai, P. N. Darma, P. A. Sejati, R. Wicaksono, H. Hayashi, and M. Takei, "Gastric functional monitoring by gastric electrical impedance tomography (geit) suit with dual-step fuzzy clustering," *Scientific Reports*, vol. 13, p. 514, Jan. 2023.

[5] Z. Xu *et al.*, "Development of a portable electrical impedance tomography system for biomedical applications," *IEEE Sensors Journal*, vol. 18, pp. 8117–8124, Oct. 2018.

[6] Y. Luo *et al.*, "Non-invasive electrical impedance tomography for multi-scale detection of liver fat content," *Theranostics*, vol. 8, no. 6, pp. 1636–1647, 2018.

[7] P. Kassanos, "Bioimpedance sensors: A tutorial," *IEEE Sensors Journal*, vol. 21, pp. 22190–22219, Oct. 2021.

[8] M. A. Kadir, A. J. Wilson, and K. S.-e. Rabbani, "A multi-frequency focused impedance measurement system based on analogue synchronous peak detection," *Frontiers in Electronics*, vol. 2, p. 791016, Dec. 2021.

[9] R. Wicaksono, M. R. Baidillah, P. N. Darma, A. Inoue, H. Tsuji, and M. Takei, "Pocket electrical impedance tomography (p-eit) system with wide impedance range buffer-mirrored current source (bmcs) with assist of filter-trained quasi-3-d method for functional gastric-shape imaging," *IEEE Transactions on Instrumentation and Measurement*, vol. 70, pp. 1–17, 2021.

[10] I. I. Nwokoye and I. F. Triantis, "A 3 mhz low-error adaptive howland current source for high-frequency bioimpedance applications," *Sensors*, vol. 24, p. 4357, July 2024.

[11] D. Yap, E. K. Y. Ma, W. Y. Oon, F. Zouari, R. W. Chan, and E. C. Wong, "Mo380: Bioconductivity measurement for electrical impedance tomography (eit) in chronic kidney disease—a non-invasive and portable monitoring approach," *Nephrology Dialysis Transplantation*, vol. 37, May 2022.

[12] X.-Y. Ke *et al.*, "Advances in electrical impedance tomography-based brain imaging," *Military Medical Research*, vol. 9, Dec. 2022.

[13] H. Liu, S. Zhao, C. Tan, and F. Dong, "A bilateral constrained image reconstruction method using electrical impedance tomography and ultrasonic measurement," *IEEE Sensors Journal*, vol. 19, pp. 9883–9895, Nov. 2019.

[14] M. Takhti and K. Odame, "Structured design methodology to achieve a high snr electrical impedance tomography," *IEEE Transactions on Biomedical Circuits and Systems*, vol. 13, pp. 364–375, Apr. 2019.

[15] V. G. Sirtoli, K. F. Morcelles, and V. C. Vincence, "Design of current sources for load common mode optimization," *Journal of Electrical Bioimpedance*, vol. 9, pp. 59–71, Dec. 2018.

[16] R. Bayford, R. Sadleir, I. Frerichs, T. I. Oh, and S. Leonhardt, "Progress in electrical impedance tomography and bioimpedance," *Physiological Measurement*, vol. 45, p. 080301, Aug. 2024.

[17] F. Pennati *et al.*, "Electrical impedance tomography: From the traditional design to the novel frontier of wearables," *Sensors*, vol. 23, p. 1182, Jan. 2023.